Plasma-graphene interaction and its effects on nanoscale patterning

Abhilash Harpale, Marco Panesi, and Huck Beng Chew*
Department of Aerospace Engineering, University of Illinois at Urbana-Champaign, Urbana, Illinois 61801, USA
(Received 31 October 2015; revised manuscript received 9 December 2015; published 11 January 2016)

Scalable and precise nanopatterning of graphene is an essential step for graphene-based device fabrication. Hydrogen-plasma reactions have been shown to narrow graphene only from the edges, or to selectively produce circular or hexagonal holes in the basal plane of graphene, but the underlying plasma-graphene chemistry is unknown. Here, we study the hydrogen-plasma etching of monolayer graphene supported on SiO_2 substrates across the range of plasma ion energies using scale-bridging molecular dynamics (MD) simulations based on reactive force-field potential. Our results uncover distinct etching mechanisms, operative within narrow ion energy windows, which fully explain the differing plasma-graphene reactions observed experimentally. Specific ion energy ranges are demonstrated for stable isotropic (∼2 eV) versus anisotropic hole growth (∼20–30 eV) within the basal plane of graphene, as well as for pure edge etching of graphene (∼1 eV). Understanding the complex plasma-graphene chemistry opens up a means for controlled patterning of graphene nanostructures.

DOI: 10.1103/PhysRevB.93.035416

I. INTRODUCTION

Graphene is the lightest and strongest known material, with extremely high thermal and electrical conductivity [1,2]. However, graphene has to be patterned to achieve its full potential. The patterning of holes in graphene or the etching of graphene edges to form nanoribbons can open a band gap for graphene transistors [3–5]. Nanoporous graphene membranes are also attractive for water filtration, gas separation, fast DNA sequencing and translocation, and energy storage [6–11]. Chemical vapor deposition methods are now able to produce high-quality, macroscopic-scale graphene sheets cheaply and in large quantities [12–14]. In comparison, scalable top-down nanoscale patterning of graphene has not achieved the same level of maturity and sophistication.

While there exists ample experimental evidence for the pattering of graphene by hydrogen-plasma treatment, the reported etching reactions and the resulting graphene nanostructures have been vastly different [15–17]. Xie *et al.* observed that a graphene sheet deposited on SiO_2 substrate and placed downstream of an active H_2-plasma chamber undergoes selective edge etching with no damage to its basal plane [15]. In contrast, Diankov *et al.* and Yang *et al.* both reported combined basal plane and edge etching of graphene by H_2-plasma treatment [16,17]. Regarding the basal plane etching of monolayer graphene, Diankov *et al.* and Yang *et al.* demonstrated isotropic and anisotropic hole growth in the basal plane of graphene, respectively, which led to the formation of circular and hexagonal holes. The plasma-graphene etching rates for all three studies were also found to be very different, ranging from 0.1 to 40 nm/min. To date, controlling the patterned graphene nanostructures by hydrogen-plasma treatment has not been achieved due to a lack of fundamental understanding of the complex hydrogen plasma-graphene chemistry.

Some have proposed that the neutral H radicals, having a density ∼1000 times that of the ions, are the primary species responsible for the plasma-graphene etching [18,19]. However, the H radicals alone cannot explain how defects within the initially pristine basal plane of graphene can continuously nucleate, nor can it account for the distinctively different plasma-etched graphene nanostructures reported experimentally. Recent mass spectrometry measurements show that the ions approaching the graphene sample downstream from the discharge can have energies as high as ∼45 eV, depending on the plasma process conditions [20]. Three possible types of ions (H^+, H_2^+, H_3^+) have been found in the H_2-plasma etching of graphene, with H_3^+ being the most prevalent. Closer to the graphene surface, these energetic ions will undergo dissociative recombination to form neutral, but energetic, H radicals. For example, two possible branching reactions for $H_3^+ + e$ are $H_2 + H$ and 3H [21,22].

Using large-scale massively parallel molecular dynamics (MD) simulations, we establish the contribution of the energetic H ions to the plasma-etching process and uncover distinct transitions in the etching mechanisms with ion energy, which fully explains the differing plasma-graphene reactions reported in the experiments [15–17]. Based on the MD simulation results, we develop a micromechanics model to predict the hole-growth response in monolayer graphene at experimental length and time scales, accounting for synergistic effects of both the energetic H ions and the H radicals. In particular, we show that selective edge etching with no damage to the basal plane occurs at ion energies of ∼1 eV, while nanopores within the graphene basal plane can only stably grow within very narrow ion energy bands of ∼2 eV for circular holes and ∼25–30 eV for hexagonal holes. Our results underscore the importance of tuning the plasma process conditions to achieve the desired nanoscale patterns.

II. COMPUTATIONAL METHODS

Our MD simulations for the energetic bombardment of H atoms on SiO_2 supported monolayer graphene are performed using LAMMPS [23]. The interatomic interactions between the Si, O, H, and C atoms are fully governed by a reactive force-field (ReaxFF) potential which allows for continuous bond breaking and reforming, as well as potential chemical and

*Author to whom all correspondence should be addressed. Email: hbchew@illinois.edu

 ©2016 American Physical Society

physical reactions involving the SiO_2 substrate [24,25]. The ReaxFF potential consists of bond-order-dependent valance terms, position-dependent charge distribution, and nonbonded van der Waals and Coulombic interactions between all atoms. The potential has been shown to accurately capture the reaction dynamics of SiO_2, C/H/O, SiC systems, including graphene hydrogenation and hydrocarbon decomposition. We have performed a series of validation studies, confirming the activation barrier energy of ∼0.47 eV for chemisorption of H on the stable top site of monolayer graphene, and the associated formation energy of ∼1.65 eV, to be in excellent agreement with values of ∼0.5 and ∼1.44 eV, respectively, from prior density functional theory (DFT) calculations [26–28]. The transition in the local hybridization state of hydrogenated graphene from sp^2 to sp^3, and the associated local deformations in the bonding structure of graphene, are also in very good agreement with prior DFT results. Specifically, at the sp^3 hybridized site, the ReaxFF (DFT) calculations show locally deformed C-C and C-H bond lengths of 1.5 Å (1.5 Å) and 1.1 Å (1.1 Å), and C-C-H and C-C-C- bond angles of 104° (101°) and 114° (115°).

We perform length-scale bridging by delineating the contributions of the edge and basal plane etching in MD and linking these processes together via a mechanistic model. Our $6.8 \times 9.8 \times 6.1\ \mathrm{nm}^3$ periodic MD simulation box comprises of a 2.1-nm-thick α-quartz (SiO_2) crystal, which is oxygen terminated, and with the (001) plane oriented normal to the vertical (z) axis. In our simulation of pristine basal plane etching, we model a periodic monolayer graphene sheet on top of SiO_2, where the in-plane dimensions of the sheet and the substrate are equal (in-plane mismatch strain of ∼0.07%). To delineate the effects of edge etching, we model a 4.2-nm (5.8 nm) wide graphene nanoribbon, which is periodic in the y (x) direction and has exposed zigzag (armchair) edges. Each of these SiO_2-graphene systems, with initial configurations depicted in Fig. 1, is then subjected to an *NVT* ensemble at a temperature of 300 °C, which is maintained by a Berendsen thermostat for 1.5 ps. We find the average distance between the C atoms in graphene and the O-terminated surface of the substrate to be 0.32 nm, which is in close agreement with the value of 0.29 nm from DFT calculations [29]. We rigidly fix the bottom 0.5-nm layer of atoms in the SiO_2 substrate throughout our simulations and designate the next 1.0-nm layer of atoms above this fixed region as the heat-bath region, which equilibrates the temperature of the remaining atoms above it. All our simulations are conducted with a fixed time step of 0.15 fs.

We accelerate the plasma-etching simulations by dividing the in-plane dimensions of the simulation box into 3×3 grids and simultaneously depositing nine H atoms randomly (one H atom within each cell) from 0.6 nm above the graphene sheet with velocities in the $-z$ direction corresponding to kinetic energy of 1–30 eV. Each of these nine impacts are independent of each other, since the impact damage is highly localized due to the small mass of the H atom. After the nine H atoms are deposited, the entire system is equilibrated without a thermostat for the first 6000 iterations (0.9 ps) to resolve the initial impact dynamics. We then switch on the thermostat in the heat-bath region for the next 16,000 iterations (2.4 ps), set to the target temperature of 300 °C using a Berendsen thermostat with a temperature damping constant of 7.5 fs, to remove the excess energy introduced by the energetic H atoms. Thereafter, the graphene sheet is quenched to the target temperature of 300 °C for a further 2000 iterations (0.3 ps). The entire bombardment cycle is then repeated for the next nine H atom impacts. Our primary interest is in the etching of the graphene sheet caused by the energetic H atoms, and not by thermal fluctuations of the equilibrium state between the bombardment events. The choice of the 3.6-ps bombardment cycle period allows us to time accelerate the etching process to simulate over ∼1800 H atom impacts (∼200 bombardment cycles) for each ion energy, which effectively represents a fluence of $\sim 2.6 \times 10^{15}\ \mathrm{ions/cm}^2$. Etching of graphene nanoribbons at incident energies of 1 eV was continued to a fluence of $\sim 4.7 \times 10^{15}\ \mathrm{ions/cm}^2$ due to the exceptionally low damage rate.

III. RESULTS

Figure 2 shows distinct transitions in the etching mechanisms with increasing ion energies for a graphene nanoribbon with exposed zigzag edges. At low ion energies of 1 eV, the H atoms can only bind to the edges of the graphene sheet to induce selective edge etching while leaving the basal plane undamaged. At ion energies of 5 eV, a large number of H atoms now bind to the top of the sheet and initiate basal plane etching. The hydrogenation of the top side of the sheet induces

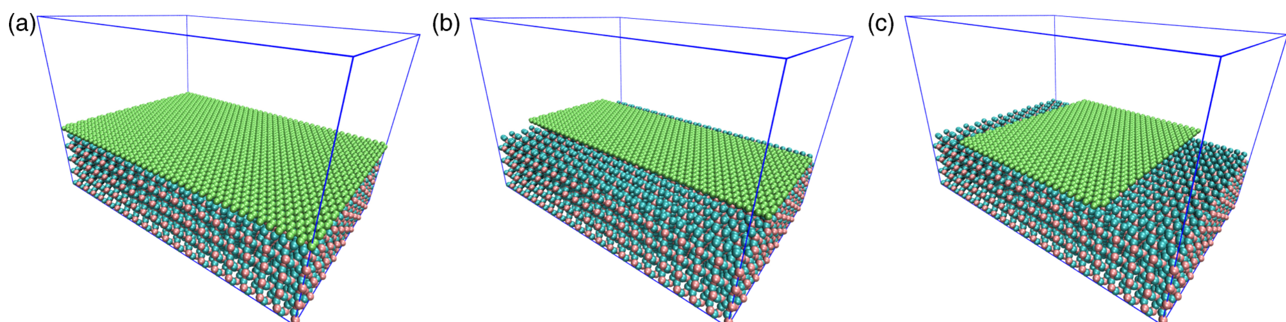

FIG. 1. Molecular dynamics modeling of the H_2-plasma etching of monolayer graphene on SiO_2 substrate. Atomic configurations for (a) fully periodic monolayer graphene without exposed edges, (b) graphene nanoribbon of 4.2 nm width with exposed zigzag edges, and (c) graphene nanoribbon of 5.8 nm width with exposed armchair edges. The C, Si, and O atoms are colored in green, pink, and blue, respectively. The simulation box, outlined in blue, is periodic in the in-plane (x-y) directions.

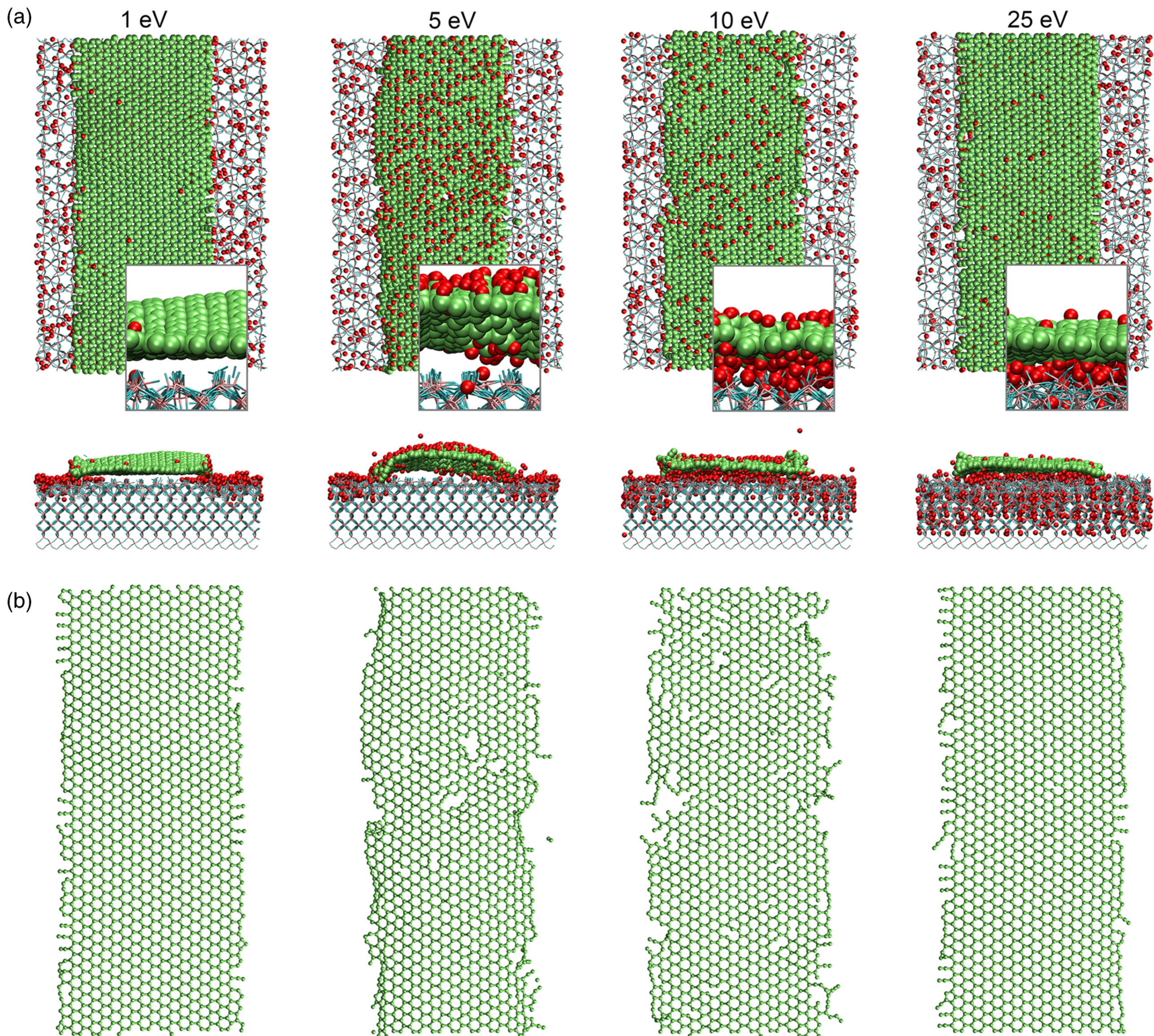

FIG. 2. Edge and basal plane etching of graphene nanoribbons with exposed zigzag edges. The bombardment of H atoms was carried out at energies of 1, 5, 10, and 25 eV. (a) Top- and side-view atomic configurations at a fluence of 2.1×10^{15} ions/cm^2, with red and green atoms denoting the H and C atoms, and interconnected lines representing SiO_2. Close-up views show the extent of hydrogenation at the top and bottom of each graphene nanoribbon. (b) Atomic configurations, corresponding to the snapshots in (a), filtered to display only the C atoms and the C-C bonds of each graphene nanoribbon.

sp^2 to sp^3 transitions in the hybridization of the C atoms; the sp^3 hybridized bond configurations causes the hybridized C atoms to deflect ~0.35 Å in the out-of-plane ($+z$) direction. At high fluences, the collective effect induces visible warping of the graphene sheet. At higher ion energies of 10 eV, H atoms have just sufficient energy to penetrate the graphene sheet and are chemisorbed on both sides of the sheet, which induces significant edge and basal plane etching; the graphene sheet remains flat due to approximately equal rates of hydrogenation of the top and bottom sides of the sheet. However, when the ion energy exceeds 25 eV, most of the H atoms now penetrate the sheet without causing damage and are embedded within the bulk SiO_2 substrate; a small fraction of H atoms which collide with the substrate atoms are reflected back and hydrogenate the bottom of the sheet, causing some basal plane damage.

A. Basal plane etching

We first isolate the contributions of basal plane etching by simulating the energetic ion bombardment of fully periodic monolayer graphene sheets, without exposed edges, on SiO_2 substrates. We quantify the extent of basal plane damage for each ion energy by defining a damage parameter D_b as the fraction of broken C-C bonds in the graphene sheet. We calculate D_b from the average coordination number of the C atoms in the current state, which accounts for reforming of previously broken C-C bonds if the bond distance decreases below the 1.7-Å cutoff distance (~20% bond stretch); $D_b = 0$ represents an undamaged sheet, while $D_b = 1$ implies full atomization of the graphene sheet with no C-C bonds remaining on the substrate. The basal plane of graphene remains nearly undamaged ($D_b \sim 0$) at ion energies of 1 eV

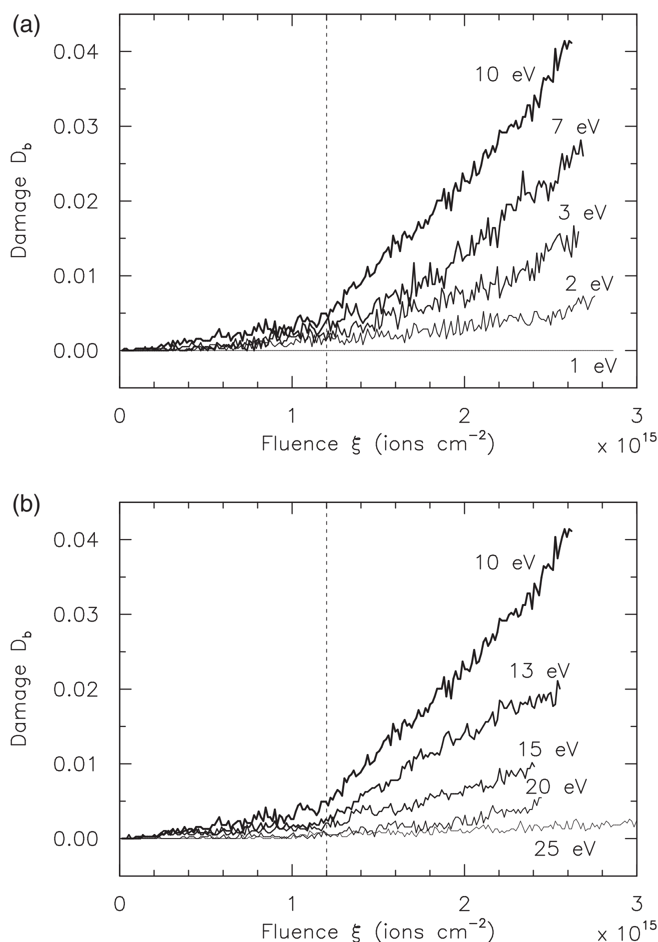

FIG. 3. Evolution of basal plane damage D_b versus ion fluence ξ for monolayer graphene sheets subjected to ion energies of (a) 1–10 eV and (b) 10–25 eV.

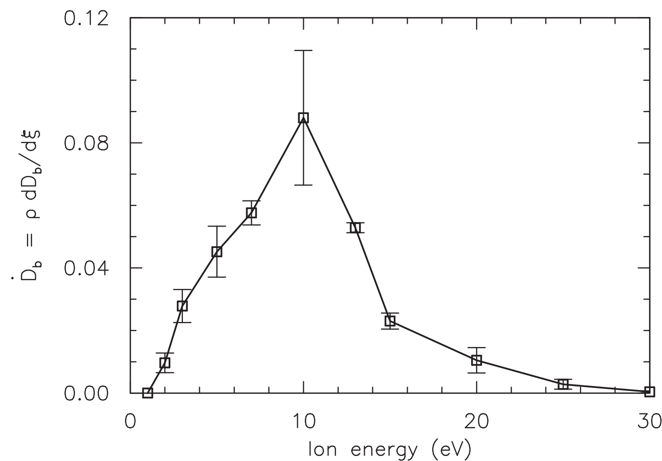

FIG. 4. Summary of the steady-state basal plane etching rate per unit area $\dot{D}_b$ versus the ion energy for monolayer graphene sheets. Error bars denote the unbiased standard error.

and 25 eV, but D_b displays a bilinear relationship with the ion fluence ξ for ion energies in between (Fig. 3): an initial gentle slope corresponding to the nucleation of defects in the basal plane, followed by an abrupt transition to a much steeper slope at $\xi \sim 1.2 \times 10^{15}$ ions/cm^2 associated with the steady-state propagation of damage from these defect sites. Neglecting the nucleation period, we summarize in Fig. 4 the steady-state basal plane etching rate per unit area, $\dot{D}_b = \rho\, dD_b/d\xi$, where $\rho = 3.8 \times 10^{15}$ cm^{-2} is the area density of C atoms in graphene. Additionally, we subdivide the graphene sheet into four quadrants and calculate $\dot{D}_b$ within each quadrant to quantify the statistical distribution of damage. Note that $\dot{D}_b$ is a nonmonotonic function of the ion energy: zero at 1 eV and below, peaks at ∼10 eV, and approaches zero again at 30 eV and beyond, since the graphene sheet becomes completely transparent to the H ions [30]. We estimate that the damage to the basal plane remains negligible up to ion energies of 90–100 eV, beyond which sputtering is observed. However, such energy levels are not present in the low-energy plasma treatment of graphene [20].

We observe that the initiation of basal plane damage requires the chemisorption of H atoms on two closest-neighbor C atoms. In this regard, three C-H bond configurations are possible [Fig. 5(a)], depending on whether the neighboring H atoms are both bonded to the top (TT) or bottom (BB) of the sheet, or one H atom on each side (TB). The TT and BB bond configurations are predominant at low ($\leqslant\sim$ 5 eV) or high ion energies ($\geqslant\sim$ 20 eV), while the TB configuration is typical at intermediate ion energy levels (∼7–15 eV). The chemisorption of H atoms to the basal plane causes sp^2 to sp^3 transitions in the hybridization of the C atoms. An isolated H atom bonded to a C atom causes the neighboring C-C bond to stretch to 1.51–1.53 Å. For C-H bond pairs in the TT or BB configurations [Fig. 5(b-i)], the C-C bond distance between these sp^3-hybridized C atoms further stretches to 1.68–1.70 Å, compared to a C-C bond length of 1.42 Å for pristine graphene. These observations are comparable to previous DFT calculations [27]. The subsequent influx of H atoms causes the breaking of neighboring C-C bonds [A-B and C-D in Figs. 5(b-ii) and 5(b-iii)] to form a C_2H_4 bond structure. The rotation of this rigid bond structure, due to its open tetrahedral configuration, causes the breaking of an additional two neighboring C-C bonds [E-F and E-G in Fig. 5(b-iii)]. With further influx of H atoms, the C_2H_4 bond structure now separates to form dangling CH_2 and CH_3 groups, and the latter breaks off due to thermal vibrations to release a CH_3 radical [Fig. 5(b-iv)]. The etching reaction is more straightforward for chemisorbed H atoms in the TB configuration, where the C-H bond pairs are on opposite sides of the graphene sheet [Fig. 5(c-i)]. The binding of an additional H atom to either one of these sp^3-hybridized C atoms breaks the neighboring C-C bonds in the process. This sp^3-hybridized C atom receives a third H atom from its neighbor to form a dangling CH_3 group [Fig. 5(c-ii)], which subsequently detaches due to thermal vibrations to release a CH_3 radical [Fig. 5(c-iii)]. In both reactions, the CH_3 radical will subsequently form CH_4 by combining with the H radicals in the plasma chamber.

We determine the extent of TT, BB, and TB bond configurations at various ion energies by calculating the average number of chemisorbed H atoms per C atom at the top and bottom of the graphene sheet, denoted by H_t and H_b, respectively. Our calculations show that both H_t and H_b linearly increase with

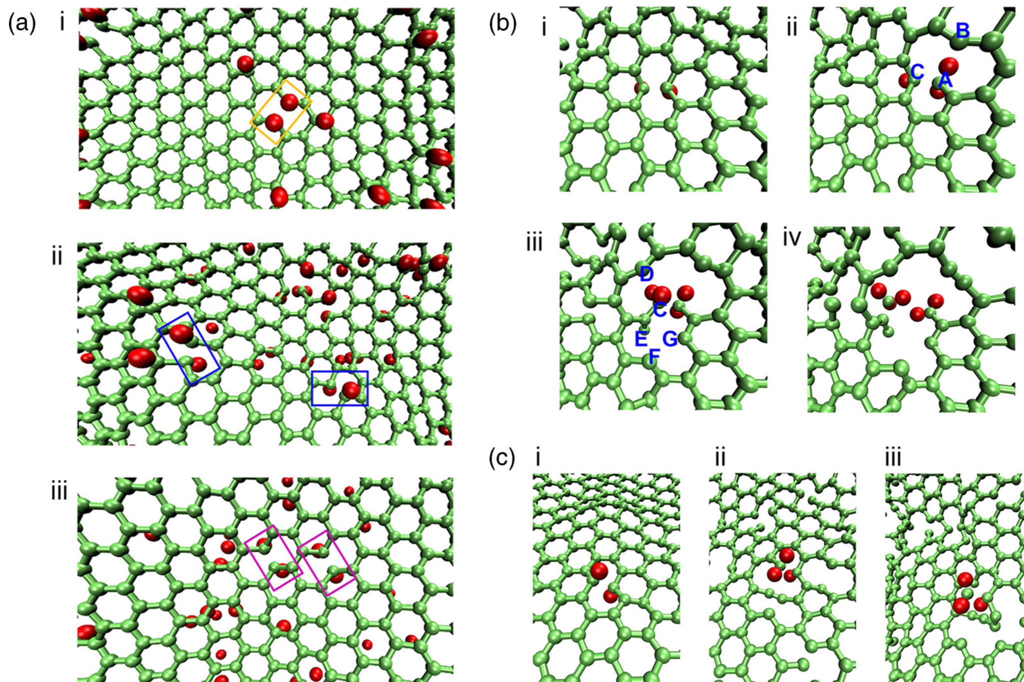

FIG. 5. Mechanisms of basal plane etching of monolayer graphene sheets. (a) Three possible configurations of C-H bond pairs on closest-neighbor C atoms to nucleate basal plane damage: (a-i) top-top, (a-ii) top-bottom, and (a-iii) bottom-bottom configurations, taken at ion energies of 5, 10, and 15 eV, respectively. (b, c) Perspective views of the basal plane etching mechanisms initiated by the chemisorption of H atoms on a pair of closest-neighbor C atoms to form C-H bond pairs on the same side of the graphene sheet (b) and on opposite sides of the graphene sheet (c).

ξ across all ion energies, and we include the respective C-H bond formation rates $\dot{H}_t = dH_t/d\xi$ (red) and $\dot{H}_b = dH_b/d\xi$ (blue), as well as the overall hydrogenation rate $\dot{H}_t + \dot{H}_b$ (black), in Fig. 6. Observe that top-surface hydrogenation dominates at lower ion energies, which promotes TT bond configurations, while bottom-surface hydrogenation is more prevalent at higher ion energies, resulting in BB bond configurations. Initiation of bottom-surface hydrogenation occurs at $\sim$3 eV, which corresponds to the DFT-calculated barrier energy of 2.50–2.86 eV for the penetration of a H atom through a graphene lattice [26,31]. Even though the overall hydrogenation rate $\dot{H}_t + \dot{H}_b$ peaks at $\sim$5 eV, the maximum basal plane etching rate $\dot{D}_b$ occurs at ion energies of 10 eV; this coincides with $\dot{H}_t \approx \dot{H}_b$, which makes the formation of TB bond configurations most likely. Considering that about five H ions are required to etch off a single C atom in either the TT or BB configuration [Fig. 5(b)], compared to about three H ions for the TB configuration [Fig. 5(c)], the etching rates will be $\sim$67% higher for the TB configuration, which explains the maximum etching rate at $\sim$10 eV.

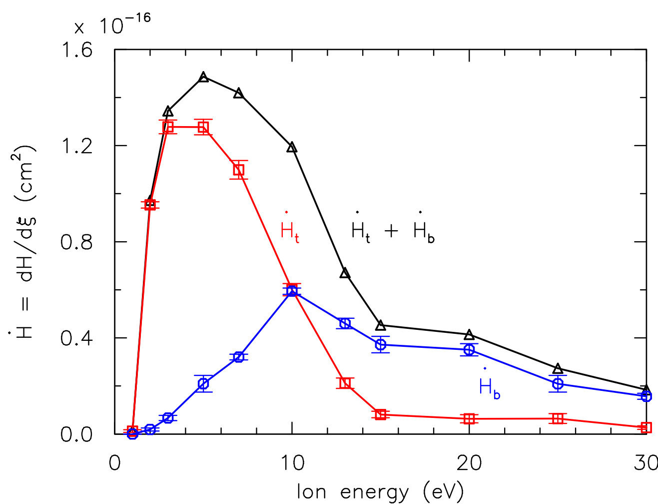

FIG. 6. Summary of the hydrogenation rates, $\dot{H}_t$ and $\dot{H}_b$, at the top and bottom surface of monolayer graphene and their combination, $\dot{H}_t + \dot{H}_b$, versus the ion energy. Error bars denote the unbiased standard error.

B. Edge etching

We next isolate the contributions of edge etching by simulating the energetic ion bombardment of graphene nanoribbons with exposed zigzag or armchair edges on SiO_2 substrates. We quantify the edge damage parameter D_e as the number of etched C atoms attributable to the presence of the exposed edges per unit edge length. The edge region is defined as the narrow strip of graphene within distance d from the boundary atoms. The choice of d will affect the accurate calculation of D_e, particularly at large ion fluences. For a strip that is too wide, basal plane etching can be expected within d. For a strip that is too narrow, some of the edge etching contribution will be neglected when damage progresses inward from the edges beyond d. In order to minimize the error from these factors, we choose $d = 6.4$ Å in all our calculations. Note that D_e is related to the calculation of the basal plane damage parameter D_b within the strip by $D_e = \rho D_b d$. Our simulations

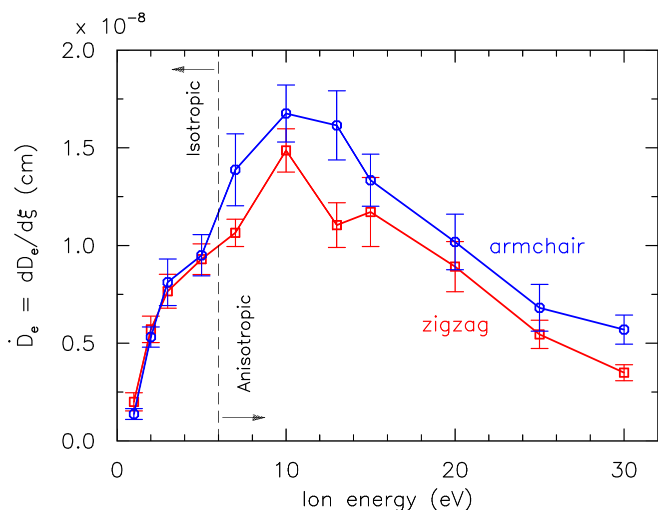

FIG. 7. Summary of the zigzag and armchair edge etching rates per unit edge length $\dot{D}_e$ versus the ion energy for graphene nanoribbons. Error bars denote the unbiased standard error.

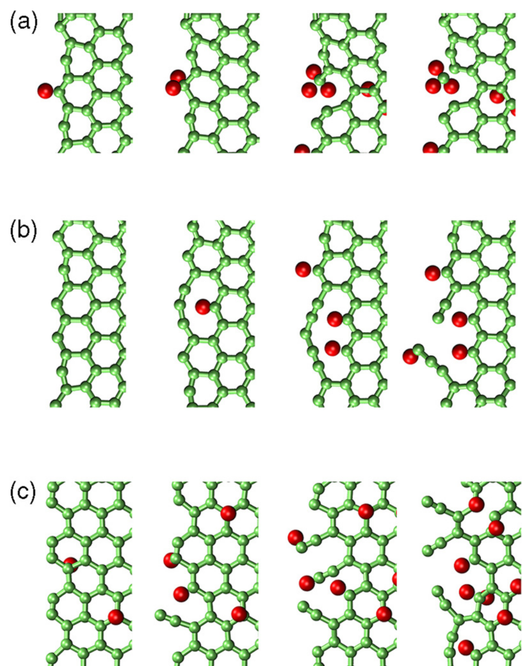

FIG. 8. Mechanisms of edge etching of graphene nanoribbons. (a, b) Zigzag edge etching: (a) formation and detachment of CH_3 by direct hydrogenation of the edge atoms, and (b) unzipping of the double-bonded edge C atoms by breaking of the inner C-C bonds. (c) Armchair edge etching: breaking of the inner C-C bonds attached to triple-bonded edge atoms.

show that D_e increases linearly with ξ for all ion energies and does not require an initial damage nucleation period, unlike basal plane etching, since the armchair or zigzag edges are pre-existing defects. However, the calculated edge-etching rates $\dot{D}_e = dD_e/d\xi$ are subjected to statistical variations, which are exacerbated by the short edge lengths modeled in MD. Hence, we perform a total of five independent simulations with different random seeds for depositing the H atoms and obtain a statistical distribution of $\dot{D}_e$ comprising ten data points for each ion energy (two edges on each side of the nanoribbon). We summarize in Fig. 7 the average zigzag (red) and armchair (blue) edge-etching rates $\dot{D}_e$ as a function of the ion energy. Similar to basal plane etching, we find $\dot{D}_e$ to be highest at 10 eV. However, we continue to observe etching at the armchair and zigzag edges at 1 eV as well as at 30 eV, which suggests that selective edge etching will occur at these ion energies with no damage to the basal plane.

Our results in Fig. 7 demonstrate distinct ion energy regimes for isotropic versus anisotropic etching. Between 1 and 5 eV, the average armchair and zigzag etching rates are similar with overlapping error bars. At ion energies of between 7 and 30 eV, however, armchair etching consistently proceeds faster than zigzag etching by $\sim$15%, suggesting that the patterned holes should indeed be hexagonal (longest to shortest diagonals in a hexagon differ by $\sim$15%) with zigzag-oriented edge structures. The shift from isotropic to anisotropic etching with increasing ion energy is explained by examining the damage mechanisms associated with zigzag and armchair etching in Fig. 8. Etching of the zigzag edges at 1 to 5 eV predominantly occurs by hydrogenation of the edge atoms, which results in the formation and subsequent detachment of CH_3 groups [Fig. 8(a)]. At ion energies greater than 5 eV, incoming H atoms have sufficient energy to break the weaker inner C-C bonds to form C-H bonds, simultaneously unzipping a chain of edge C atoms [Fig. 8(b)]. In contrast, etching of the armchair edges involves some component of momentum-induced breaking of inner C-C bonds at all ion energies [Fig. 8(c)], since the higher stability of the triple-bonded C-C edge atoms inhibits direct etching of these atoms by hydrogenation [32,33]. Therefore, there are two competing effects: (a) higher reactivity of the zigzag edge atoms compared to armchair, due to the presence of edge states near the Fermi level [34], and (b) lower bond dissociation energy of the inner C-C bonds attached to the edge atoms in armchair edge compared to zigzag [35]. At ion energies of 5 eV and below, both these effects compensate each other to cause similar etching rates. At higher ion energies where the effect of (b) dominates, armchair etching proceeds faster than zigzag etching.

IV. MICROMECHANICS MODELING

Our MD simulations capture the kinetics of early-stage plasma etching and have to be scaled to experimentally relevant length and time scales. Ultimately, the hole-growth kinetics will be governed by the synergistic effects of basal plane and edge etching caused by the energetic H ions; the etching reactions should involve the denser H radicals as well.

Consider the radial expansion of a circular hole in the basal plane of monolayer graphene from radius R to $R + dR$, resulting in the removal of $(\rho 2\pi R)dR$ carbon atoms by combined basal plane and edge etching. Edge etching by the energetic H ions will contribute to the removal of $(\dot{D}_e\, 2\pi R)d\xi$ carbon atoms, while the cumulative basal plane etching contribution will remove $(\dot{D}_b\, \xi\, 2\pi R)dR$ carbon atoms. Here, we neglect the contribution of the initial damage nucleation period of $\xi = 1.2 \times 10^{15}\ \text{ions/cm}^2$ for $\dot{D}_b$, which is short relative to the estimated experimental etching duration of $\sim 10^{17}$ to $10^{18}\ \text{ions/cm}^2$.

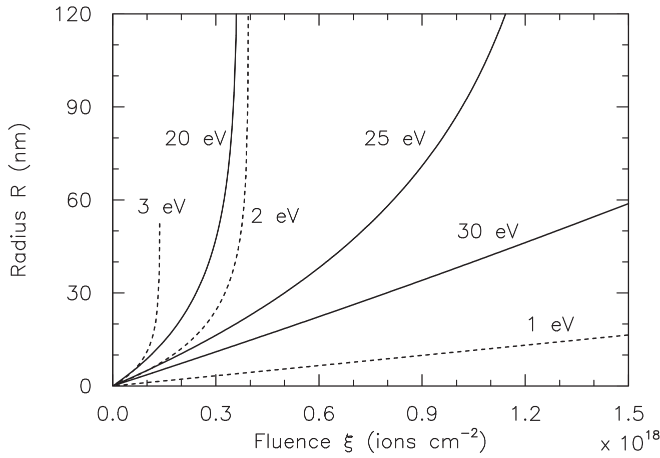

FIG. 9. Kinetics of hole growth in the graphene basal plane. Hole-growth radius R versus the ion fluence ξ caused by combined basal plane and edge etching, accounting for the synergistic effects of H ions and radicals. Isotropic and anisotropic hole growth denoted by dashed and solid lines, respectively.

In addition to the energetic H ions, the neutral H radicals will also contribute to the etching process. The H radicals have an equivalent thermal energy of ~0.026 eV at a temperature of 300 °C but have a density ~1000 times that of the energetic ions. We have separately exposed zigzag- and armchair-edged monolayer graphene to a relatively high fluence of H radicals of up to 1.2×10^{16} radicals/cm^2. The simulations were performed by randomly inserting H atoms above the graphene/substrate in our simulation box with a kinetic energy of 0.1 eV (velocity in the $-z$ direction) and maintaining the temperature of our system at 300 °C with a Berendsen thermostat. We observe no hydrogenation of the basal plane of graphene even after the long exposure time. We therefore conclude that the thermal H radicals have insufficient energy to bind with the basal plane and hence will have limited bearing on basal plane etching prior to substantial hole growth. Assuming an ion to radical density ratio of 1:1000, the chemisorption rate of H radicals at the armchair and zigzag edges of graphene will be orders-of-magnitude higher than that of the energetic ions, causing the exposed edges to be fully hydrogenated to form CH_2 edge-type bonds. In our repeated simulation runs (five sets for each edge type), we do not observe any CH_3 bonds forming at the hydrogenated zigzag or armchair edges, nor do we find any C-C bond breaking attributable to the presence of these H radicals. This implies that the thermal radicals at 300 °C have insufficient energy to break the respective C-C double or triple bonds for the zigzag and armchair edges. Nevertheless, it is conceivable that these H radicals will hydrogenate and eventually etch off the more unstable dangling bonds created at the edges by the energetic H ions. Assuming that the thermal H radicals will accelerate the edge etching damage caused by the energetic ions by a prefactor α, we equate the total number of etched C atoms for radial expansion of the hole with the contributions from both basal plane and edge etching, and integrate to obtain

$$R = -\frac{\alpha \dot{D}_e}{\dot{D}_b} \ln\left(1 - \frac{\dot{D}_b \xi}{\rho}\right). \quad (1)$$

Both the basal plane and edge etching rates ($\dot{D}_b$, $\dot{D}_e$) for different H ion energies are obtained directly from our MD simulations. However, the prefactor α is unknown. Here, we estimate α based on the three distinct edge-etching mechanisms identified in Figs. 8(a)–8(c), herein termed as mechanisms 1–3. In mechanism 1 [Fig. 8(a)], the sequential bonding of three H atoms leads to the etching of a single zigzag edge C atom. However, the graphene edge atoms will already be CH_2 terminated in the presence of thermal H radicals. Therefore, only a single energetic H atom will be required to etch off the edge C atom, and the actual edge etching rate for mechanism 1 will be $\sim 3\dot{D}_e$, i.e., $\alpha = \sim 3$. In mechanism 2 [Fig. 8(b)], the breaking of each inner C-C bond attached to double-bonded zigzag edge atoms creates a strip of C atoms. Subsequent bombardment breaks off this strip to form dangling C-C bonds. Considering that these dangling C-C bonds will be etched off by thermal H radicals, we estimate α for mechanism 2 to range from ~5/2 to 8/3. In mechanism 3 [Fig. 8(c)], the breaking of each inner C-C bond attached to triple-bonded armchair edge atoms creates a dangling chain of two C atoms which will be etched off by thermal radicals, implying that $\alpha = \sim 3$. For simplicity, we assume $\alpha = 3$ in Eq. (1) for mechanisms 1–3.

Results from this simple model demonstrate narrow ion energy bands of ≤~2 eV and ≥~20 eV where circular and hexagonal holes, respectively, can stably grow (Fig. 9).

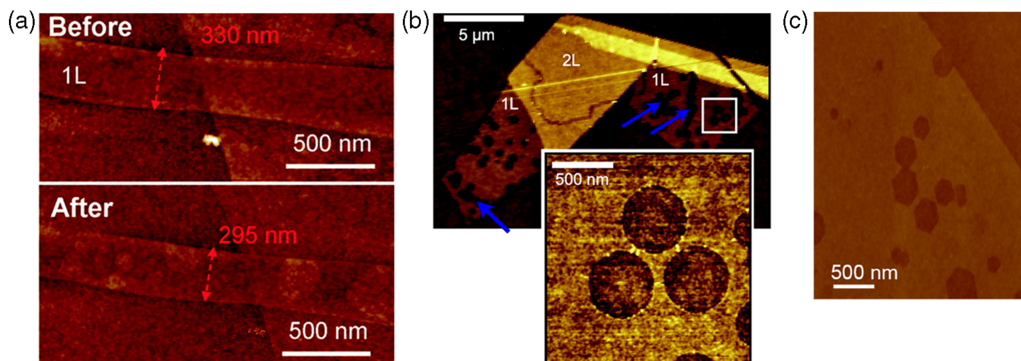

FIG. 10. AFM topography imaging of three distinct graphene patterns from H_2-plasma etching of monolayer graphene on SiO_2 substrates [15–17], reproduced with permission: (a) selective edge etching, and the formation of (b) circular and (c) hexagonal holes in the basal plane, resulting from estimated H ion energies of ~1, ~2, and ~25 eV, respectively.

Within the intermediate energy range of ∼3–15 eV, basal plane etching proceeds so rapidly that the sheet simply disintegrates before distinct holes can develop. These results can explain the differing patterned graphene nanostructures in existing experiments (Fig. 10). Low ion energies of ∼1 eV are responsible for the selective edge etching of monolayer graphene [Fig. 10(a)], as also evidenced by the low plasma power (20 W) and long downstream distance (40 cm) of the graphene sample [15]. At shorter downstream distance (30 cm) from the plasma source (20 W), slightly higher ion energies of ∼2 eV are expected, which leads to combined edge and basal plane etching [16]; the isotropic etching creates circular holes in the graphene basal plane [Fig. 10(b)]. Our model further predicts that etching occurs rapidly at 2 eV and quickly becomes unstable at ∼3 eV. Interestingly, this is also reflected in the fast 40 nm/min etch rate reported experimentally, as well as the extensive, and at times unstable, basal plane etching seen in parts of the graphene sheet [arrows in Fig. 10(b)]. In fact, the same study reported complete disintegration of the sheet when shifted ∼1 cm closer to the plasma source. At higher plasma power (50 W), stable anisotropic etching in the basal plane with rates of 6 nm/min were observed [17]. These etching reactions were likely caused by ion energies of ∼25 eV, which resulted in zigzag-terminated hexagonal holes [Fig. 10(c)].

V. DISCUSSION AND CONCLUSION

Our ReaxFF-based MD simulations allow for chemical reactions between the Si-C-H-O atoms. Contrary to previous speculations [16], however, we find that the SiO_2 substrate does not chemically participate in the plasma-etching process, except for a small number of instances where we observe H_2O and O_2 molecules. However, the substrate is responsible for the reflection of some of the more energetic H atoms which penetrate the sheet; the reflected atoms eventually hydrogenate the bottom side of the sheet and contribute to the etching process. We delineate the effects of the SiO_2 substrate by performing the bombardment of energetic H atoms on a suspended monolayer graphene sheet by holding the C atoms near the supercell boundary fixed to prevent the sheet from displacing due to the H atom impacts. Our results consistently show lower overall hydrogenation rates ($\dot{H}_t + \dot{H}_b$) for the suspended graphene sheet than for the SiO_2 supported graphene [Fig. 11(a)]. The range of ion energies which cause basal plane etching ($\dot{D}_b$) is reduced from ∼2–30 eV to ∼2–20 eV in the absence of the substrate [Fig. 11(b)]. Radial distribution function (RDF) analysis for H-H species within the substrate [Fig. 11(c)] shows that the fraction of H_2 molecules increases with bombardment energy, indicating a H-H recombination reaction within the substrate bulk. While the H atoms trapped within the SiO_2 voids are relatively stable and have very low diffusivity [36], the H_2 molecules can diffuse out of the substrate but are inert and do not cause any damage to the graphene sheet. Finally, we remark that the substrate also plays a vital role in the thermal transport of H radicals along the substrate's surface to hydrogenate the armchair or zigzag edges of the monolayer graphene sheet—∼60% of the CH and CH_2 edge bonds in our H radical simulations, described in Sec. IV, are formed in this fashion.

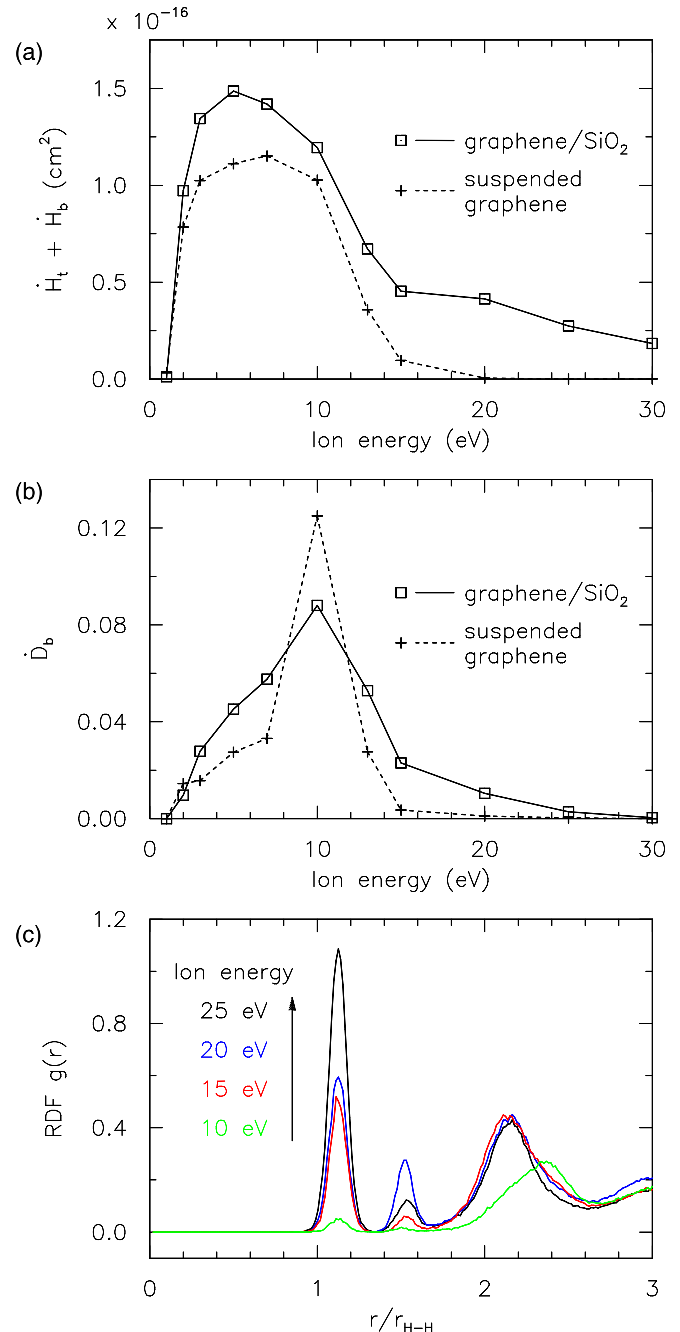

FIG. 11. Role of the SiO_2 substrate. (a, b) Comparison of the total hydrogenation rates (a) and the basal plane etching rates (b) between freestanding graphene and graphene supported on SiO_2. (c) Radial distribution function analysis for H-H species within the SiO_2 substrate. The interatomic separation distance r is normalized with respect to the equilibrium bond length of a H_2 molecule $r_{H-H} = 0.741$ Å.

Our MD simulations are performed at a fixed temperature of 300 °C, which approximately corresponds to the optimal H_2-plasma-etching rate in the experiments [16,17]. We remark that the observation of a maximum reaction rate at a given temperature (300 °C for monolayer graphene) is typical of reactions between gaseous species and hot solid surfaces in which volatile products are formed [37]. Increasing temperature

could increase the rate of hydrogen ion/radical recombination into molecules, leading to a suppression of the hydrogen ion/radical density at the graphene sample. Furthermore, the rate of hydrogenation as well as dehydrogenation of graphene is well known to depend on temperature, which could influence the basal plane and edge-etching rates [38]. Elucidating these effects and their contribution to the temperature-dependent plasma-etching process is a subject of future work.

In conclusion, we have identified specific H ion energy regimes responsible for selective edge etching of monolayer graphene without basal plane damage (∼1 eV) and for stable growth of circular (∼2 eV) or hexagonal holes (∼20–30 eV) in the graphene basal plane. The distinctive etching mechanisms operative within these narrow ion energy regimes fully explain the differing plasma-graphene reactions observed experimentally. Understanding these plasma-graphene reactions will enable controlled patterning of graphene nanostructures, which has important implications for graphene-based device fabrication.

ACKNOWLEDGMENTS

This work was supported by the AE Multidisciplinary Initiative (UIUC), as well as the National Science Foundation (Award No. NSF-CMMI-1538162). Computational time was provided by TACC (Award No. TG-MSS130007) and the Blue Waters sustained-petascale computing project, which is supported by the National Science Foundation (Awards No. OCI-0725070 and No. ACI-1238993) and the State of Illinois, USA. Blue Waters is a joint effort of the University of Illinois at Urbana-Champaign and its National Center for Supercomputing Applications.

[1] A. K. Geim and K. S. Novoselov, The rise of graphene, Nat. Mater. **6**, 183 (2007).

[2] F. Bonaccorso, Z. Sun, T. Hasan, and A. C. Ferrari, Graphene photonics and optoelectronics, Nat. Photonics **4**, 611 (2010).

[3] M. Dvorak, W. Oswald, and Z. Wu, Opening by patterning graphene, Sci. Rep. **3**, 2289 (2013).

[4] Y.-W. Son, M. L. Cohen, and S. G. Louie, Energy gaps in graphene nanoribbons, Phys. Rev. Lett. **97**, 216803 (2006).

[5] Y.-W. Son, M. L. Cohen, and S. G. Louie, Half-metallic graphene nanoribbons, Nature (London) **444**, 347 (2006).

[6] S. P. Surwade, S. N. Smirnov, I. V Vlassiouk, R. R. Unocic, G. M. Veith, S. Dai, and S. M. Mahurin, Water desalination using nanoporous single-layer graphene, Nat. Nanotechnol. **10**, 459 (2015).

[7] D. Cohen-Tanugi and J. C. Grossman, Water desalination across nanoporous graphene, Nano Lett. **12**, 3602 (2012).

[8] A. W. Hauser and P. Schwerdtfeger, Methane-selective nanoporous graphene membranes for gas purification, Phys. Chem. Chem. Phys. **14**, 13292 (2012).

[9] S. P. Koenig, L. Wang, J. Pellegrino, and J. S. Bunch, Selective molecular sieving through porous graphene, Nat. Nanotechnol. **7**, 728 (2012).

[10] H. W. C. Postma, Rapid sequencing of individual DNA molecules in graphene nanogaps, Nano Lett. **10**, 420 (2010).

[11] M. F. El-Kady and R. B. Kaner, Scalable fabrication of high-power graphene micro-supercapacitors for flexible and on-chip energy storage, Nat. Commun. **4**, 1475 (2013).

[12] A. Reina, X. Jia, J. Ho, D. Nezich, H. Son, V. Bulovic, M. S. Dresselhaus, and J. Kong, Few-layer graphene films on arbitrary substrates by chemical vapor deposition, Nano Lett. **9**, 30 (2009).

[13] X. Li, C. W. Magnuson, A. Venugopal, R. M. Tromp, J. B. Hannon, E. M. Vogel, L. Colombo, and R. S. Ruoff, Large-area graphene single crystals grown by low-pressure chemical vapor deposition of methane on copper, J. Am. Chem. Soc. **133**, 2816 (2011).

[14] A. Harpale, M. Panesi, and H. B. Chew, Surface-to-bulk diffusion of isolated versus interacting C atoms in Ni(111) and Cu(111) substrates: A first principle investigation, J. Chem. Phys. **142**, 061101 (2015).

[15] L. Xie, L. Jiao, and H. Dai, Selective etching of graphene edges by hydrogen plasma, J. Am. Chem. Soc. **132**, 14751 (2010).

[16] G. Diankov, M. Neumann, and D. Goldhaber-Gordon, Extreme monolayer-selectivity of hydrogen-plasma reactions with graphene, ACS Nano **7**, 1324 (2013).

[17] R. Yang, L. Zhang, Y. Wang, Z. Shi, D. Shi, H. Gao, E. Wang, and G. Zhang, An anisotropic etching effect in the graphene basal plane, Adv. Mater. **22**, 4014 (2010).

[18] N. Skoro, N. Puac, S. Lazovic, U. Cvelbar, G. Kokkoris, and E. Gogolides, Characterization and global modelling of low-pressure hydrogen-based RF plasmas suitable for surface cleaning processes, J. Phys. D: Appl. Phys. **46**, 475206 (2013).

[19] A. Davydova, E. Despiau-Pujo, G. Cunge, and D. B. Graves, Etching mechanisms of graphene nanoribbons in downstream H_2 plasmas: insights from molecular dynamics simulations, J. Phys. D: Appl. Phys. **48**, 195202 (2015).

[20] A. Felten, D. McManus, C. Rice, L. Nittler, J. J. Pireaux, and C. Casiraghi, Insight into hydrogenation of graphene: Effect of hydrogen plasma chemistry, Appl. Phys. Lett. **105**, 183104 (2014).

[21] M. A. Cazalilla, N. Lorente, R. D. Muino, J. P. Gauyacq, D. Teillet-Billy, and P. M. Echenique, Theory of Auger neutralization and deexcitation of slow ions at metal surfaces, Phys. Rev. B **58**, 13991 (1998).

[22] S. Datz, G. Sundstrom, C. Biedermann, L. Brostrom, H. Danared, S. Mannervik, J. R. Mowat, and M. Larsson, Branching processes in the dissociative recombination of H3+, Phys. Rev. Lett. **74**, 896 (1995).

[23] S. Plimpton, Fast parallel algorithms for short-range molecular dynamics, J. Comput. Phys. **117**, 1 (1995).

[24] A. C. T. van Duin, S. Dasgupta, F. Lorant, and W. A. Goddard, ReaxFF: A reactive force field for hydrocarbons, J. Phys. Chem. A **105**, 9396 (2001).

[25] D. A. Newsome, D. Sengupta, H. Foroutan, M. F. Russo, and A. C. T. van Duin, Oxidation of silicon carbide by O_2 and H_2O: A ReaxFF reactive molecular dynamics study, part I, J. Phys. Chem. C **116**, 16111 (2012).

[26] E. Despiau-Pujo, A. Davydova, G. Cunge, L. Delfour, L. Magaud, and D. B. Graves, Elementary processes of H_2 plasma-graphene interaction: A combined molecular dynamics and

density functional theory study, J. Appl. Phys. **113**, 114302 (2013).

[27] D. W. Boukhvalov, M. I. Katsnelson, and A. I. Lichtenstein, Hydrogen on graphene: Electronic structure, total energy, structural distortions and magnetism from first-principles calculations, Phys. Rev. B **77**, 035427 (2008).

[28] V. V. Ivanovskaya, A. Zobelli, D. Teillet-Billy, N. Rougeau, V. Sidis, and P. R. Briddon, Hydrogen adsorption on graphene: a first principles study, Eur. Phys. J. B **76**, 481 (2010).

[29] T. C. Nguyen, M. Otani, and S. Okada, Semiconducting Electronic Property of Graphene Adsorbed on (0001) Surfaces of SiO_2, Phys. Rev. Lett. **106**, 106801 (2011).

[30] S. Hu, M. Lozada-Hidalgo, F. C. Wang, A. Mishchenko, F. Schedin, R. R. Nair, E. W. Hill, D. W. Boukhvalov, M. I. Katsnelson, R. A. W. Dryfe, I. V. Grigorieva, H. Wu, and A. K. Geim, Geim, Proton transport through one-atom-thick crystals, Nature (London) **516**, 227 (2014).

[31] M. Miao, M. B. Nardelli, Q. Wang, and Y. Liu, First principles study of the permeability of graphene to hydrogen atoms, Phys. Chem. Chem. Phys. **15**, 16132 (2013).

[32] Y. Liu, A. Dobrinsky, and B. I. Yakobson, Graphene edge from armchair to zigzag: The origins of nanotube chirality?, Phys. Rev. Lett. **105**, 235502 (2010).

[33] S. Okada, Energetics of carbon peapods: Elliptical deformation of nanotubes and aggregation of encapsulated C60, Phys. Rev. B **77**, 235419 (2008).

[34] D. Jiang, B. G. Sumpter, and S. Dai, Unique chemical reactivity of a graphene nanoribbon's zigzag edge, J. Chem. Phys. **126**, 134701 (2007).

[35] C. J. Russo and J. A. Golovchenko, Atom-by-atom nucleation and growth of graphene nanopores, Proc. Natl. Acad. Sci. USA **109**, 5953 (2012).

[36] R. W. Lee, R. C. Frank, and D. E. Swets, Diffusion of hydrogen and deuterium in fused quartz, J. Chem. Phys. **36**, 1062 (1962).

[37] D. E. Rosner, High-temperature gas-solid reactions, Annu. Rev. Mater. Sci. **2**, 573 (1972).

[38] Z. Luo, T. Yu, K. J. Kim, Z. Ni, Y. You, S. Lim, Z. Shen, S. Wang, and J. Lin, Thickness-dependent reversible hydrogenation of graphene layers, ACS Nano **3**, 1781 (2009).